Defects and mass transport in rutile-structured fluorides. I. Experiment

S. Ling* and A. S. Nowick
Henry Krumb School of Mines, Columbia University, New York, New York 10027
(Received 26 January 1989)

A study of low-temperature dielectric relaxation of Er^{3+}- and Y^{3+}-doped MnF_2 crystals in orientations both parallel and perpendicular to the tetragonal c axis shows the presence of relaxation peaks with very low activation energies E. Specifically, for both dopants, a prominent peak is found in parallel-oriented samples with $E \sim 6$ meV and in perpendicular orientation with $E = 37$ meV for Er^{3+} and $E = 46$ meV for Y^{3+} doping. Such low E values are probably too small to be controlled by lattice migration of a defect. With the aid of computer-simulation calculations, these peaks were interpreted as resulting from a stable low-symmetry configuration of a dopant-F_i pair (F_i is the fluorine-ion interstitial), which allows dipole reorientation by motions involving small fractions of lattice distances. It is then concluded that the intrinsic defect in this crystal is of the anion Frenkel, and not the Schottky, type, as had been proposed earlier. Electrical-conductivity measurements on pure and doped MnF_2 were then interpreted in terms of this defect model to obtain $H_f = 3.56 \pm 0.02$ eV for the formation enthalpy of the anion Frenkel defect, $H_m = 0.10$ eV for the migration enthalpy of the F_i, and $H_A = 1.1$ eV for the dopant-F_i association enthalpy. The results agree well with the computer-simulation calculations given in the following paper.

I. INTRODUCTION

In the study of point defects in ionic crystals, the most extensive work has been carried out on crystals with cubic symmetry, notably, the alkali halides, silver halides, and akaline-earth fluorides.[1–7] Crystals both pure and doped with aliovalent impurities have been studied. The various techniques employed in these studies include electrical conductivity, diffusion, EPR, dielectric and anelastic relaxation, and, with the advent of powerful computers, computer-simulation calculations. In ionic materials of lower-than-cubic symmetry, some of these experimental techniques can be even more versatile for identifying appropriate defect structures. The reason is that many physical properties of the system (e.g., electrical conductivity, dielectric constant) have a larger number of independent components as a result of the more anisotropic nature of the system.[8] Thus, by carrying out measurements on noncubic crystals in different orientations, more information about defect structure and transport can be derived.

The fluorides that possess the tetragonal rutile structure (see Fig. 1), such as MgF_2, MnF_2, and ZnF_2, are particularly well suited to such studies. These materials are good ionic crystals with large band gaps and are chemically similar to the cubic alkaline-earth fluorides, e.g., CaF_2 and SrF_2, which have been extensively studied. In the past few years there have been quite a number of investigations related to the defect structure of such crystals, including electrical conductivity,[9–11] internal friction,[12,13] dielectric relaxation,[14,15] and atomic diffusion.[16]

From their study of electrical conductivity of MnF_2 and MgF_2 doped with various cation dopants, Park and Nowick[9] tentatively proposed that the intrinsic defect was of the anion Frenkel type. On the other hand, Catlow *et al.*,[17] using computer-simulation calculations, reported a distinctly lower energy per defect for the Schottky defect than for the anion Frenkel in these crystals. The computer program used, however, was the earlier HADES II code, which was designed for cubic crystals, as well as with cruder F^--F^- potentials than are currently available. In short, the nature of the dominant intrinsic disorder in these crystals has remained quite unclear.

In the present work, MnF_2 single crystals, both pure and doped (with Er^{3+} and Y^{3+}, respectively), and to a lesser extent Sc^{3+}-doped MgF_2, have been studied with a combination of high-temperature electrical-conductivity and low-temperature dielectric relaxation measurements. Full use was made of the anisotropic nature of these crystals by studying these properties both parallel and perpendicular to the crystallographic c axis. It will be shown that these measurements give valuable information about both the defect structure and transport properties of the crystals, which also lead to the identification of the predominant intrinsic defect as the anion Frenkel

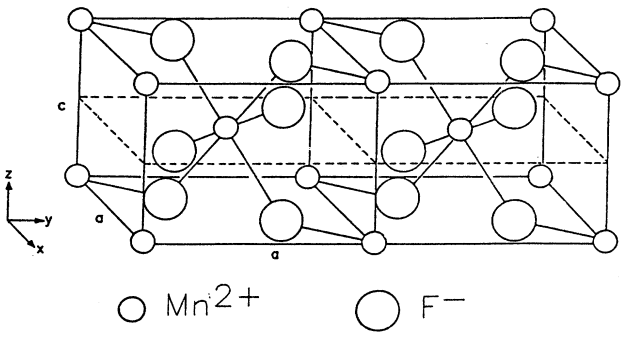

FIG. 1. The tetragonal rutile structure of the MnF_2 crystal.

type. The following paper[18] then presents the results of computer-simulation calculations for these systems, using both a code more suitable to anisotropic materials as well as more reliable fluorine-fluorine potentials.

II. THEORY

A. Dielectric loss

Dielectric loss[19,20] can arise from defects that have a lower symmetry than that of the crystal in which they reside. Such defects possess several crystallographically equivalent orientations, among which they may reorient preferentially in the presence of an electric field. If the electric field is sinusoidal with angular frequency ω, one or more peaks will usually occur in that dielectric loss, $\tan\delta$, which obey the well-known Debye equation

$$\tan\delta=\epsilon''/\epsilon'=(\delta\epsilon/\epsilon_\infty)\omega\tau/(1+\omega^2\tau^2) \quad (1)$$

where ϵ'',ϵ' are the imaginary and real parts of the complex dielectric constants, respectively, ϵ_∞ is the relative dielectric constant at high frequencies, $\delta\epsilon$ is the relaxation of the dielectric constant, and τ^{-1} is the rate of relaxation. For a uniaxial (e.g., a tetragonal) crystal, expressions of the type of Eq. (1) may be separately obtained for orientations that are parallel ($\|$) and perpendicular ($\perp$) to the crystallographic c axis, and each of the parameters $\delta\epsilon$, ϵ_∞, and τ, are, in general, different for the two orientations.

Equation (1) yields a symmetric peak in a plot of $\tan\delta$ versus $\ln\omega$ centered about the value ω_m given by

$$\omega_m=\tau^{-1} . \quad (2)$$

If the defects reorient by jumping over a barrier, τ^{-1} can be written in the classical Arrhenius form

$$\tau^{-1}=\tau_0^{-1}\exp(-E/k_BT) , \quad (3)$$

where τ_0^{-1} is the preexponential factor, E is the activation energy, and k_BT has its usual meaning. Equation (1) can then be rewritten into the form

$$T\tan\delta\propto\operatorname{sech}[E/k_BT+\ln(\omega\tau_0)] \quad (4)$$

which yields a symmetric peak in a plot of $T\tan\delta$ versus $1/T$. The peak height is given by

$$(T\tan\delta)_{\max}=N_dp^2/2\alpha\epsilon_0\epsilon_\infty k_B . \quad (5)$$

Here, N_d is the concentration of the defects (in number per volume), ϵ_0 is the permittivity of free space, and α is a geometric factor, which is 1 and 2 in the $\|$ and $\perp$ orientations, respectively. Finally, p is the component of the defect dipole moment parallel to the c axis or the component in the basal plane, for the $\|$ and $\perp$ orientations, respectively. When measured at two angular frequencies, say ω_1 and ω_2, the shift of the peak in $1/T$, $\Delta(1/T)$, is given by the following equation:

$$E\Delta(1/T)=k_B\ln(\omega_2/\omega_1) , \quad (6)$$

from which the activation energy E may be obtained.

B. Electrical conductivity

The electrical conductivity[1-3] of an ionic system has contributions from all charged defect carriers. It is often that one defect species in the system predominates, in which case the conductivity is given by

$$\sigma=CN_0q\mu , \quad (7)$$

where C is the concentration of the predominating defect charge carrier expressed as a mole fraction, q and μ are its charge and mobility, respectively, and N_0 is the host-cation concentration. Again, there are different values for μ, and therefore for σ, in the $\|$ and $\perp$ orientations. For samples doped with aliovalent impurities, the electrical conductivity has the well-known three-stage temperature dependence: namely the intrinsic, the extrinsic dissociation, and the extrinsic associated regions (also known as stages I, II, and III, respectively). In general, the conductivity in each temperature stage assumes the Arrhenius temperature dependence

$$\sigma T=A\exp(-H/k_BT) , \quad (8)$$

where H is the activation enthalpy and A is the preexponential, which may be given by

$$A=X(q^2N_0Zd^2W_0/\beta k_B) , \quad (9)$$

Here, Z is the number of equivalent jumps of the defect, β is a geometric factor, d is the appropriate component of the jump distance of the migrating defect, and W_0 is the jump-frequency preexponential that includes the entropy of activation factor. For the $\|$ orientation, $\beta=2$ and d is the component of jump distance along the c axis; for the $\perp$ orientation, $\beta=4$ and d is the component of jump distance in the basal plane. The quantity X is a factor that we call the "effective concentration" of the defect carrier; it is defined in such a way that in stage II it is the actual defect concentration (as a mole fraction). The expressions for both X and H are different in each of the three temperature stages.

Both H and X can be derived for specific defect models. We will now proceed to write down their expressions assuming that the intrinsic disorder is anion Frenkel in nature. (A similar derivation may be carried out to obtain H and X for the Schottky defect model.)

If the intrinsic disorder is the anion Frenkel pair, the fluorine vacancy and the fluorine interstitial, designated by V_{F} and F_i, respectively, the corresponding intrinsic mass-action equation is

$$[\mathrm{F}_i][V_{\mathrm{F}}]=\exp(-G_f/k_BT) , \quad (10)$$

where $[\mathrm{F}_i]$ and $[V_{\mathrm{F}}]$ denote concentrations of F_i and V_{F}, respectively, expressed as mole fractions, and G_f is the formation free energy of the Frenkel pair given by

$$G_f=H_f-TS_f , \quad (11)$$

where H_f and S_f are the corresponding enthalpy and entropy values. From Eqs. (10) and (11) we readily obtain the expressions for H and X of the intrinsic region, stage I, given in Table I. Here, H_m is the migration enthalpy of the faster-migrating defect, which we will assume to be

TABLE I. Expressions for H and X for the three conductivity stages, based on anion Frenkel model. H_f and S_f are given by Eq. (11), H_A and S_A are corresponding values for association, H_m equals the migration enthalpy of the fluorine interstitial (it may be different for $\parallel$ and $\perp$ orientation), and C_D equals the total dopant concentration.

Stage	H	X
I	$H_f/2+H_m$	$\exp(S_f/2k_B)$
II	H_m	C_D
III	$H_A/2+H_m$	$(C_D/Z')^{1/2}\exp(S_A/2k_B)$

the fluorine interstitial.

At lower temperatures, in the region of stage II, the trivalent cation dopant must be compensated by F_i defects. In the absence of association, the values of H and X are clearly those given in the second row of Table I. Finally, at still lower temperatures, association sets in, for which the mass-action equation is

$$[F_i][D]/[DF_i]=(1/Z')\exp(-G_A/k_BT)\ , \tag{12}$$

where $[F_i]$, $[D]$, and $[DF_i]$ denote the mole-fractional concentrations of fluorine interstitials, isolated dopants, and pairs, respectively, Z' is the number of equivalent orientations of the pair, and G_A is the association free energy of the pair that obeys an equation analogous to (11). In addition, one can also write down the following equations representing charge neutrality and mass conservation:

$$[D]=[F_i]\ , \tag{13}$$

$$[D]+[DF_i]=C_D\ , \tag{14}$$

where C_D is the total dopant concentration. In the usual way, with the aid of Eqs. (12)–(14), the expressions for H and X for stage III, given in Table I, are obtained.

III. EXPERIMENTAL METHODS

The materials used in this study were mainly MnF_2 single crystals. The crystals used were grown in this laboratory by the Bridgman-Stockbarger technique in a purified argon atmosphere.[21] One pure, one Er-doped, and one Y-doped crystal were grown. The dopants were grown in by adding their fluorides before melting. For comparison purpose, a Sc-doped MgF_2 crystal was also acquired from Optovac Co. Chemical analysis (carried out at Johnson-Matthey Chemicals, Ltd. England) showed that the dopants concentrations of the MnF_2 crystals were 100 and 70 at. ppm for the Er- and Y-doped crystals, respectively, while that of the MgF_2 crystal was 20 at. ppm of Sc. Thin plates of the crystals were cut in such a way that the normal to a plate was either parallel ($\parallel$ sample) or perpendicular ($\perp$ sample) to the tetragonal axis (c axis). The samples were designated in such a way to indicate both the dopant identity as well as the sample orientation, and unless otherwise specified, indicate a MnF_2 sample. Thus a $\parallel$-Er sample indicates an Er-doped MnF_2 sample that has its normal parallel to the c axis. The dimension of a sample was typically $1.2\times1.2\times0.12$ cm^3.

Silver paint (Engelhard flexible silver coating no. 16) was applied to the samples in a three-terminal configuration: a central electrode and an outer guard ring on one face, and a full electrode on the other. The electrodes were then cured by heating slightly in air with the aid of a 150-W General Electric spot light.

Both MnF_2 and MgF_2 crystals were subjected to the dielectric-loss study. In this measurement, the sample was placed inside a Janis Research Super Varitemp cryostat, and the temperature varied between 3 K and room temperature. The sample temperature was monitored and controlled by a Lake Shore type-DRC80C temperature controller with a silicon-diode sensor. The MnF_2 crystals were also subjected to the electrical-conductance study. In this measurement the sample was placed inside an air-tight fused-quartz chamber containing a purified helium atmosphere. The temperature range covered was mostly from room temperature to 700 °C, but to 900 °C in the case of the pure MnF_2 samples. The temperature was monitored with a Pt/(Pt+10% Rh) thermocouple placed near the sample.

Both dielectric-loss and conductance measurements were made using an automated bridge assembly (Carl Andeen Associates), which is an automated version of the General Radio type-1615-A bridge. Measurements were made at 17 different frequencies covering a range from 10 Hz to 100 kHz. The dielectric-loss measurements of the Y-doped MnF_2 samples, however, were made at only 1- and 5-kHz frequencies. The electrical conductance is analyzed with the ac complex-impedance method to separate the bulk conductance, with which the lattice conductivity can be calculated, from that due to other effects.[22–24] Figure 2(a) shows an idealized equivalent circuit of the sample, in which each parallel RC circuit represents one process contributing to the overall conductance. Figure 2(b) shows the complex-impedance diagram of this circuit, with the negative imaginary part Z'' plotted against the real part Z'. The higher-frequency

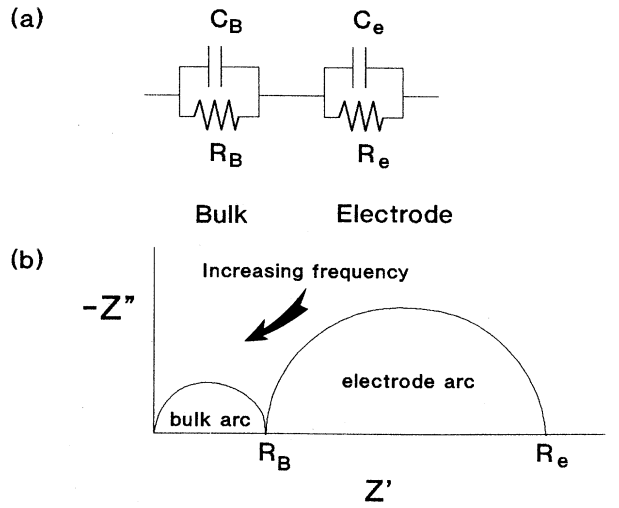

FIG. 2. Schematic diagrams of (a) the equivalent circuits representing the sample, and (b) the corresponding complex-impedance diagram.

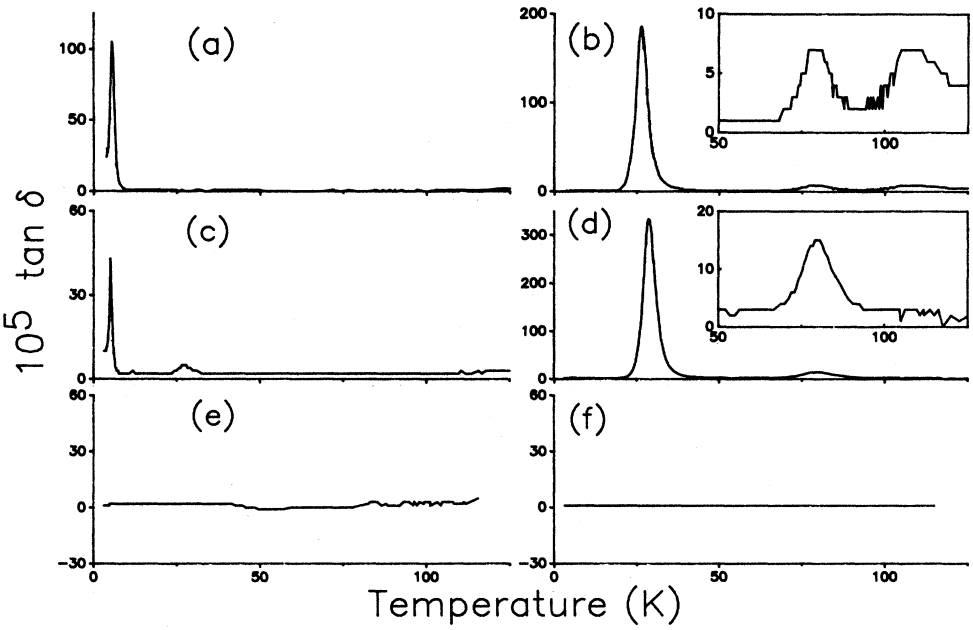

FIG. 3. The dielectric-loss spectra of MnF_2 single crystals measured at 1 kHz: (a) ||-Er, (b) ⊥-Er, (c) ||-Y, (d) ⊥-Y, (e) ||-pure, and (f) ⊥-pure. The insets of (b) and (d) magnified the small peaks at higher temperature in their respective crystals.

arc is due to the bulk effects, and the low-frequency one to the electrode effects. In reality, the electrode behavior is usually not so simple.[22,25] The important point here is that the bulk resistance R_B can be obtained from the intersection of either arc with the real axis.

IV. RESULTS

The results obtained from dielectric-loss and electrical conductivity measurements are described below.

A. ac dielectric loss

Both the MgF_2 and the MnF_2 crystals were studied with the dielectric-loss technique. No peak was observed in the Sc-doped MgF_2 sample, nor in the pure MnF_2 samples. Several low-temperature loss peaks, on the other hand, were observed in the doped MnF_2 samples. Figure 3 shows the dielectric-loss spectra (measured at 1 kHz frequency) of the pure and doped MnF_2 between 3 and 150 K in both || and ⊥ orientations. It can be seen that the spectra of all the doped samples display some similar features: a prominent peak at about 26 K in the ⊥ orientation, and another at about 5 K in the || orientation. In addition, the ⊥-Er sample had two smaller peaks trailing the main peak at higher temperatures, whereas the ⊥-Y sample has only one. The ||-Y sample, on the other hand, showed a small peak at about 26 K, which had no analogue in the ||-Er sample. Henceforth we shall refer to all peaks by their temperatures at 1 kHz.

Figures 4(a) and 4(b) show, respectively, the $T\tan\delta$ versus $1/T$ plots of the ⊥ 26.0-K and the || 5.5-K peaks observed in the Er-doped MnF_2, both measured at 1 and 5 kHz frequencies. Their activation energy E can thus be calculated from the frequency shift by Eq. (6), and their τ_0 values from the location of the peak by Eqs. (2) and (3). This calculation was straightforward for the ⊥ 26.0-K peak, which is symmetric and deviates little from an ideal Debye peak given by Eq. (4). The same thing, however, cannot be said about the || 5.5-K peak, which is lopsided and does not have a constant frequency shift, especially at the low-temperature side. A rough estimation of its activation energy is nevertheless obtained from the average frequency shift at the high-temperature side of this peak, and its τ_0 value from the peak location at 1 kHz. Similar observations and calculations were made for the Y-doped MnF_2. The peak parameters thus obtained are listed in Table II.

The height of the small dielectric-loss peaks observed in the doped samples at higher temperatures are not large

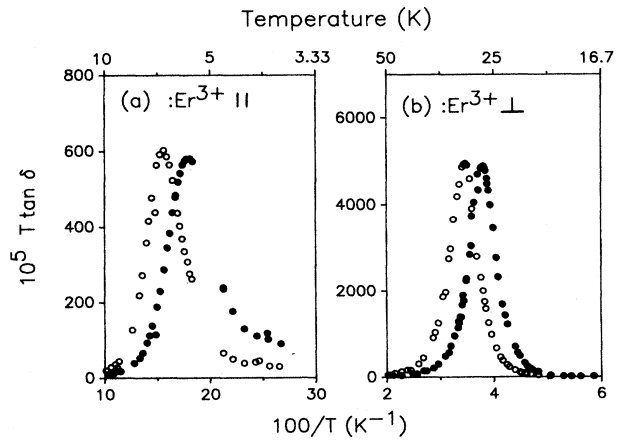

FIG. 4. Plot of $T\tan\delta$ vs $1/T$ for the dielectric-loss peaks observed in Er^{3+}-doped MnF_2 crystals, ●, measured at 1 kHz; ○ at 5 kHz. (a) || 5.5-K and (b) ⊥ 26.0-K peaks.

TABLE II. Summary of the various parameters of the dielectric loss peaks observed in the Er- and Y-doped MnF_2 crystals.

Dopant	T_{max} (K)	$10^5(tan\delta)_{max}$	E (meV)	τ_0^{-1} (s^{-1})
		Parallel		
Y^{3+}	4.8	41	7.2[a]	9.4×10^{10}
	27.5	3		
Er^{3+}	5.5	104	7.5[a]	3.2×10^{10}
		Perpendicular		
Y^{3+}	28.5	331	46.4	8.5×10^{11}
	79.5	12	144	7.6×10^{12}
Er^{3+}	26.0	185	37.1	8.5×10^{10}
	79.0	6	149	1.6×10^{13}
	108.0	4	167	3.5×10^{11}

[a]These activation energies are obtained from the average frequency shift at the high-temperature side of the lopsided low-temperature dielectric-loss peaks (see Fig. 4).

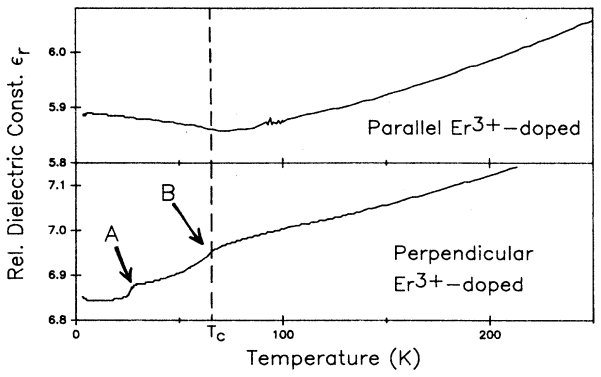

FIG. 6. Plots of relative dielectric constant ϵ_r of Er^{3+}-doped samples as a function of temperature for both the $\|$ and $\perp$ orientations. The antiferromagnetic transition of MnF_2 at $T_c=67$ K is indicated in the diagram with a vertical dashed line.

enough to allow for accurate analysis. They do, however, seem to have constant frequency shifts consistent with Eq. (6), which was used to obtain an estimate of their peak parameters listed in Table II.

The activation energy of the 5.5-K peak in $\|$-Er MnF_2 was obtained with greater accuracy with Eq. (3) in the following manner. Since the measurements on this sample were made over a range of frequencies, the peak can be plotted as $T\tan\delta$ versus $\ln\omega$ instead of versus $1/T$, as shown in Fig. 4. The temperature-dependent relaxation rate τ^{-1} is then obtained from the location of the peak by Eq. (2) for various temperatures. The result is shown in Fig. 5 as a plot of τ^{-1} versus $1/T$. It can be seen that at low temperature τ^{-1} goes roughly as T, whereas at higher temperature it obeys an Arrhenius relationship. In other words, τ^{-1} goes as $AT+\nu_0\exp(-E/k_BT)$. The dashed curve in Fig. 5 is obtained by fitting this equation to the experimental data. The values of the best-fitted parameters are $A=107.9$ K^{-1}, $\nu_0=8.75\times10^9$ s^{-1}, and $E=6.00$ meV. These are slightly different from those listed in Table II, which is not unexpected. It is not surprising that such a temperature-dependent behavior of τ^{-1} is observed for this low-temperature dielectric-loss peak. In fact, this phenomena had been reported for several other systems.[26,27] and is attributed to the onset, at very low temperatures, of single-phonon-assisted tunneling as the mechanism for the reorientation of the defect complex involved.

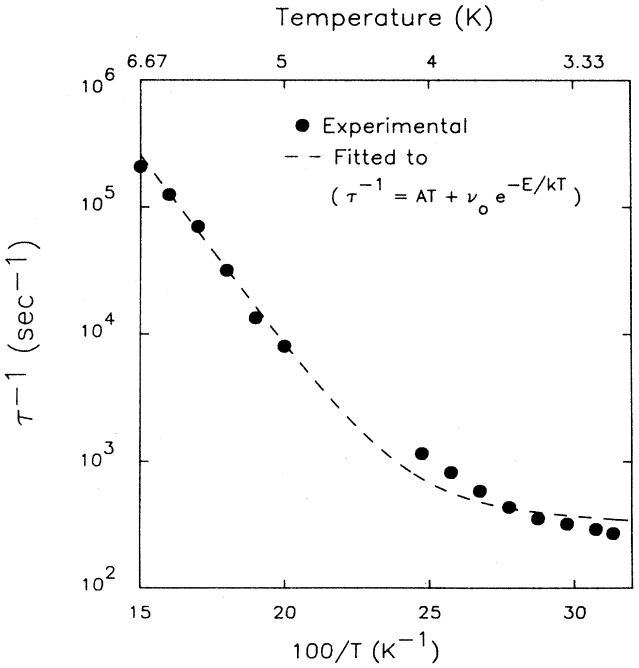

FIG. 5. Plot of τ^{-1} vs $1/T$ for the 5.5-K dielectric-loss peak observed in the $\|$-Er MnF_2 crystal. The dashed curve is obtained by fitting the equation $\tau^{-1}=AT+\nu_0\exp(-E/k_BT)$ to the experimental data, with $A=107.9$ K^{-1}, $\nu_0=8.75\times10^9$ s^{-1}, and $E=6.00$ meV.

Figure 6 shows the plots of the relative dielectric constant, which was obtained from the measured capacitances, versus temperature for the Er-doped MnF_2. It can be seen that there are anomalies in these curves. The anomalies at about 67 K, i.e., the minimum in the $\|$ direction and the inflection in the $\perp$ direction labeled "*B*," were common to all MnF_2 samples. The anomaly at about 26 K, i.e., the inflection in the $\perp$ direction labeled "*A*," on the other hand, was observed only in the Er- and Y-doped samples. It is noted that 67 K is the well-known MnF_2 antiferromagnetic transition temperature,[28] consequently, it is believed that the 67-K anomalous behavior of the dielectric constant observed here is associated with this phase transition. The 26-K anomalous behavior, on the other hand, is believed to be associated with the 26–28-K $\perp$ dielectric-loss peaks in the doped samples.

B. Electrical conductivity

The frequency-dependent complex impedance of the doped MnF_2 samples was measured from room temperature up to 700 °C, and that of the pure MnF_2 up to

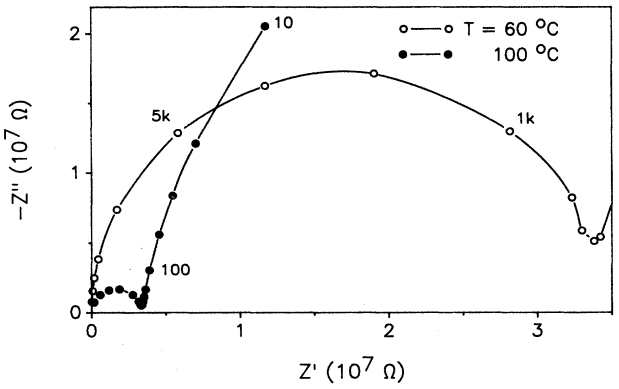

FIG. 7. Complex-impedance plots of ⊥-Er-doped MnF_2 crystal measured at 60 and 100 °C. Some data points are labeled with their measurement frequencies.

900 °C. They were, in general, consistent with the equivalent circuit shown in Fig. 2. Figure 7 shows typical complex-impedance plots measured for a ⊥-Er sample at two different temperatures. These plots show a high-frequency arc near the origin that corresponds to the bulk process, and a depressed low-frequency arc (only the beginning part of which is seen in the plots shown) that corresponds to the electrode process. The doped samples showed a well-defined bulk arc from room temperature up to 600 °C. Above 600 °C the bulk arc moved beyond 100 kHz (which is the high-frequency limit of our equipment), rendering the extraction of bulk resistance impossible. The pure samples did not show a bulk arc until approximately 300 °C, which then remained well defined up to 900 °C.

The electrical conductivities thus obtained from the complex-impedance analysis as functions of temperature are then shown in Fig. 8 as $\log_{10}(\sigma T)$ versus $1/T$. It is clear that at the lower temperature the doped samples, except the ⊥-Y sample, had conductivities several orders of magnitude higher than that of the pure ones. This indicates that the doping was successful, and that the conductivities observed were controlled by the dopants in the solid solution.

The doped MnF_2 samples all showed well developed low-temperature stages. These are assigned to stage III for reasons to be shown in Sec. V. The stage-III regions of both ||- and ⊥-Er-doped samples showed similar slopes and yielded the same value of 0.64 eV for H_{III}, even though the conductivities of the ⊥ sample were about twice that of the || one. The conductivity curve of the ||-Y sample was close to, and parallel to, that of the Er-doped samples, yielding a $H_{III}=0.65$ eV. The curve of the ⊥-Y sample, on the other hand, showed a very different behavior. Its magnitude was much lower than that of the other doped samples; in fact, at 150 °C the conductivity of this sample was about 4 orders of magnitude lower than that of the ||-Y sample. It also has a much steeper slope, resulting in a much higher H_{III} of 1.20 eV. At temperatures slightly above 150 °C, the conductivity curves for the Er-doped and ||-Y samples started to bend over, apparently into stage II, the extrinsic dissociation region. This stage, however, was not well

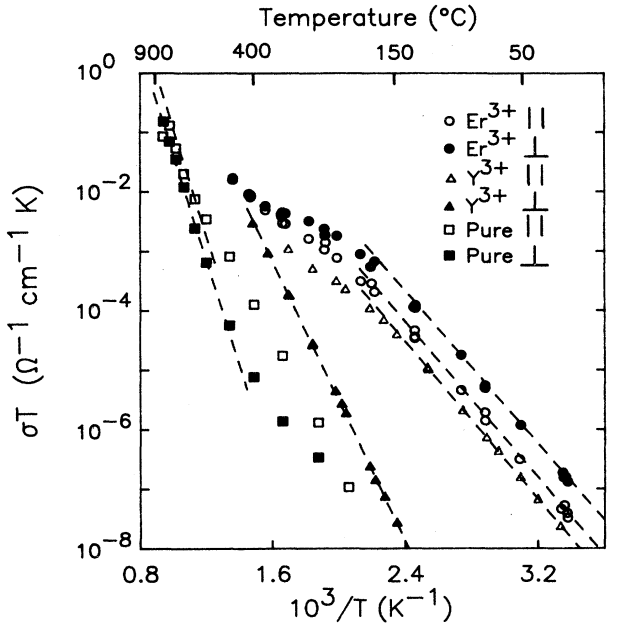

FIG. 8. Plot of σT vs $1/T$ for pure and Er- and Y-doped MnF_2 crystals, both in the || and ⊥ orientation.

defined for these samples. No such bending over was observed for the ⊥-Y sample. To check these observations on the doped samples, we measured four additional samples, one each for both orientations and for both dopants. The same kinds of behavior were observed.

The conductivities of the pure MnF_2 samples were several orders of magnitude lower than that of the doped samples throughout the temperature range covered. This was taken as an indication of the high degree of purity of these samples. The ⊥ sample showed a well-defined stage above 450 °C, and the || one above 650 °C. Their conductivity curves came close together at about 650 °C, such that they both had similar magnitudes and slopes between 650 and 900 °C. This raised the possibility that the high-temperature stage corresponds to stage I, the intrinsic region. Unfortunately, the usual way of identifying stage I—by the joining of the curves for samples with different dopant concentrations at elevated temperature—was not applicable here because of the limited number of samples available, as well as the failure to observe the first arc above 600 °C for doped samples. Instead, this claim will be further supported in Sec. V by analysis of the preexponentials.

The activation enthalpies H and preexponentials A of the various samples were determined simply by laying down a ruler on the straight regions of the conductivity plots; they are listed in Table III. Also listed in this table are the effective concentrations X calculated from Eq. (9), which will be discussed later.

The pure MnF_2 samples suffered an irreversible increase in conductivity when heated above 600 °C (see Fig. 9), especially for the || orientation. Irreversibilities were not observed in the doped samples up to 700 °C. This effect is believed to be due to the contamination of the samples by trace amounts of oxygen in the helium gas

TABLE III. Summary of the activation enthalpies and preexponentials from the conductivity plots for Er-doped, Y-doped, and pure MnF_2.

Dopant	H_I (eV)	A_I[a]	X_I	H_{III} (eV)	A_{III}[a]	X_{III}
			Parallel			
Er^{3+}				0.64	4.20×10^{3}	2.03×10^{-3}
Y^{3+}				0.65	2.47×10^{3}	1.19×10^{-3}
Pure	~1.89	2.76×10^{8}	133			
			Perpendicular			
Er^{3+}				0.64	1.21×10^{4}	2.70×10^{-3}
Y^{3+}				1.20	3.89×10^{6}	0.87×10^{0}
Pure	~1.86	6.65×10^{7}	15			

[a]The dimension for the preexponential is $\Omega^{-1}\,cm^{-1}\,K$.

used to fill the sample chamber, which seemed to be present despite our efforts to purify the helium gas.

V. DISCUSSION

In this section the dielectric-loss data will be examined first in order to determine the defect complexes that caused the relaxation peaks found in the doped MnF_2 crystals. We will concentrate on the prominent peaks (which are at roughly 5 K in the $\|$ direction and 26–28 K in the $\perp$ direction, respectively) in this discussion. The conductivity data will then be examined to determine what are the predominant charge carriers and their migration mechanisms. The atomic configurations about the defects, as obtained from computer-simulation calculations,[18] are used to provide possible defect models for this study. A basic assumption made in this discussion, that the aliovalent impurities are compensated by one member or the other of the intrinsic defect, is generally accepted from an energetic viewpoint, and is also substantiated by the study of other ionic crystals.

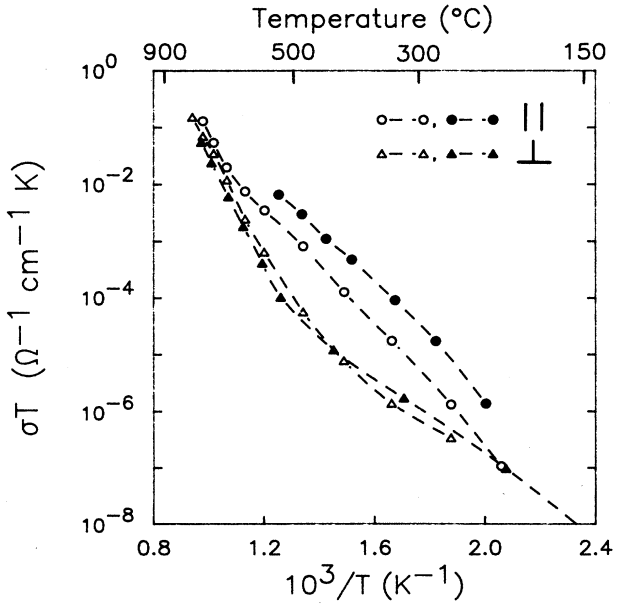

FIG. 9. Plot of σT vs $1/T$ for two pure MnF_2 crystals showing the change in σ resulting from heating to high temperatures. ○ and △ denote the data of the as-prepared sample, ●, and ▲ the data obtained on the second run, presumably after oxygen contamination.

Since the various peaks were observed only in the doped MnF_2 samples, one can conclude that these peaks are the manifestation of defect complexes involving the aliovalent dopants. These peaks are observed at cryogenic temperatures, and with very low activation energies (in the meV range). Thus it is unlikely that they are caused by defect jumps on the scale of the lattice separation. Instead it is more likely that they are caused by the reorientation of some "off-center" (more generally, "off-symmetry") type of defect configuration through a fraction of a lattice distance.[26] Figure 4 shows, aside from the low-temperature side of the $\|$ 5-K peaks, that the relaxations causing the prominent peaks obey Eq. (4). This implies that these peaks are due to simple defect complexes, such as a pair formed by the dopant and its compensating defect. The peaks in the $\perp$ samples occurred at higher temperatures and had higher relaxation energies than those in the $\|$ samples, indicating that they are due to different and independent relaxation modes of the same defect. This is, therefore, a case of a "frozen-free split" relaxation phenomenon.[29]

There are several possible simple defect complexes involving the substitutional aliovalent dopants D that may give rise to these observed peaks.

(1) Off-center D: This would have several equivalent lattice sites, and a net dipole moment.

(2) The DV_{Mn} charged pair: If the predominant intrinsic disorder were of the Schottky type, every two dopant ions would be compensated by a manganese-ion vacancy, V_{Mn}. A vacancy and a dopant ion could then be bound together to form this defect pair, which carries an effective negative charge.

(3) The DF_i neutral pair: If the predominant intrinsic disorder were of anion Frenkel type, D would be compensated by an F_i, and the two could associate to form this pair as in Eq. (12).

The off-center D is not a likely center to account for the observed peaks. In other systems where relaxation due to off-center ions has been observed the ions involved

are invariably smaller than the host ions, which presumably give them room to go off center.[26] In the systems studied here, the ionic radii of Er^{3+} and Y^{3+} are 0.88 and 0.89 Å, respectively, which are actually larger than the 0.80-Å radius of the host Mn^{2+} cation.

The charged pair, DV_{Mn}, is not a likely possibility either. The calculations carried out by Cormack *et al.*[18] for this defect pair show that it retains its symmetry about the ⟨111⟩ axis, and does not form an off-symmetry-type defect complex. As a result, the vacancy would have to jump among its crystallographically equivalent sites about the dopant in order for the pair to reorient. The energy involved in such a vacancy jump over a lattice distance is typically several tenths of eV, which is too high to account for the observed energies, which are in the meV range (see Table II).

The neutral pair involving the fluorine interstitial DF_i, on the other hand, can explain the various observations made on these peaks. The computer-simulation calculations for this defect system show that the F_i of the defect pair pushes one of its neighboring fluorine ions, which also sits next to the D, off its lattice site to form a split interstitial (shown in Fig. 10 for the case of an Er^{3+} dopant). This results in two interstitial F^- ions, which are displaced slightly and asymmetrically to the opposite sides of the (001) plane that contains the Er ion. They are also located at different distances from the $(1\bar{1}0)$ diagonal plane passing through the Er ion. This configuration thus constitutes a triclinic defect. By the crystal symmetry, there two interstitial ions also have respective equivalent positions across the (001) as well as across the $(1\bar{1}0)$ planes. [The equivalent positions across the $(1\bar{1}0)$ diagonal plane are indicated by the arrows in Fig. 10.] Thus, the defect configuration shown in Fig. 10 is capable of reorienting its dipole moment through small

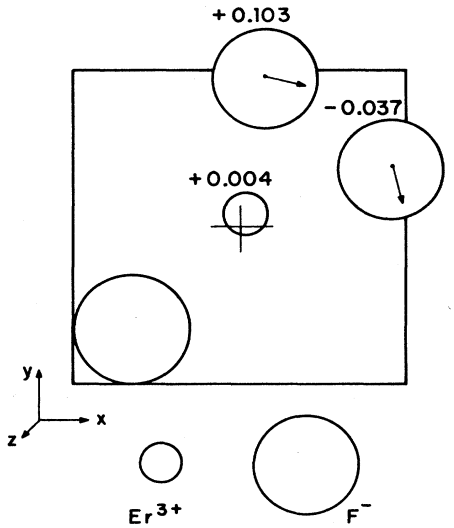

FIG. 10. The fluorine split-interstitial configuration of an ErF_i pair in the MnF_2 system. The (001) plane containing the dopant is the plane of the page. The numbers associated with the ions indicate their respective displacement from this plane. The end of arrows mark the respective equivalent sites of the two F_i's across the $(1\bar{1}0)$ diagonal plane that passes through the dopant.

motions both ∥ and ⊥ to the c axis. The two fluorine ions and the central dopant can give rise to the two desired relaxation modes in the following manner. At low temperatures they can flip to their respective equivalent positions across the (001) plane with a very low activation energy, giving rise to the ∥ 5-K peaks. The very small jump distance and the low activation energy could then allow phonon-assisted tunneling of the two fluorine ions through the energy barrier, giving rise to the observed temperature dependence of the jump rate τ^{-1}, shown in Fig. 5. At higher temperatures (approximately above 10 K) this motion takes place so rapidly that the mean locations of both fluorine ions may be regarded as being on the (001) plane. They can then reorient within the (001) plane in the manner indicated by the arrows in Fig. 10 with a higher activation energy. This process gives rise to the perpendicular peaks at 26–28 K.

It is interesting to note that calculations made on the Sc-doped MgF_2 system resulted in similar split fluorine interstitials about the substitutional Sc, except that the two fluorine ions were found to be symmetric about both the (001) and the $(1\bar{1}0)$ planes containing the Sc.[18] This implies that the ScF_i pair cannot give rise to the kind of low-temperature dielectric-loss peaks found in the doped MnF_2 crystals, which is consistent with our failure to observe any low-temperature relaxation in Sc-doped MgF_2.

Assuming the same dopant concentrations in both ∥ and ⊥ samples prepared from the same crystal, the ratio of the components of dipole moment, $p_\parallel/p_\perp$, can be calculated from the heights of observed peaks utilizing Eq. (5). From Fig. 6, the values of ϵ_∞ of MnF_2 are 5.9 at 5 K in the ∥ orientation and 6.9 at 26 K in the ⊥ orientation, respectively. Using these values, this ratio is found to be 0.23 and 0.09 for the Er- and Y-doped MnF_2 samples, respectively. The simulation calculations[18] give the atomic arrangement about the defects, from which the dipole moments can be calculated. The $p_\parallel/p_\perp$ ratios are then found to be 0.61 and 0.41 for the ErF_i and YF_i pairs, respectively. It should be noted that the computer-simulation calculations of ionic locations are very sensitive to the potentials used,[30] which puts a limit on the precision of the calculated results, so that the calculated ratio should only be viewed as a rough estimate. Even though not in quantitative agreement, both the experimental and simulation results agree that $p_\parallel$ is less than $p_\perp$.

The smaller dielectric-loss peaks found in the doped samples at higher temperatures are probably due to some higher-order defect complexes involving the cation dopants. Their low activation energies again make them likely to be the manifestation of some off-symmetry type of defect complexes. At this moment we do not have candidate models for them, although it is possible that the small 27.5-K peak for the ∥-Y sample may be simply a manifestation of the very large ⊥-Y peak due to a slight misorientation of the sample.

One of the goals of this work is to resolve the earlier controversy about the nature of the predominant intrinsic disorder in these systems, i.e., to determine whether it is of the Schottky or anion Frenkel type. The above analysis of the dielectric relaxation peaks has shown that

the defect pair present in the MnF_2 samples is one containing fluorine interstitials, and not the manganese vacancy. This means that the compensating defect of the dopant is F_i, which can be present only if the intrinsic defect is the anion Frenkel pair. Thus, an important and unexpected corollary that can be drawn from the above analysis of the dielectric-loss data is that the predominant intrinsic defect of crystalline MnF_2 is the anion Frenkel defect. The more refined computer-simulation calculations of intrinsic defect-formation energies by Cormack *et al.*[18] now support this conclusion.

We now turn to the conductivity results. Since the intrinsic defect of MnF_2 crystal is the anion Frenkel pair, the predominant charge carriers in the Er^{3+}- or Y^{3+}-doped samples are fluorine interstitials that compensate the cation dopant. The values of the effective concentration X can then be calculated from the preexponentials A using Eq. (9). The constants used in this calculation are $Z=8$, $W_0=10^{13}$ s^{-1}, and $d=1.65$ and 3.52 Å for the $\|$ and $\perp$ orientations, respectively. The values of d used here are based on the assumption that F_i migrates by the interstitialcy mechanism shown in Fig. 11, which will later be shown to be the case. The effective concentrations thus calculated are listed in Table III. Since the nominal concentrations of Er and Y in the doped crystals are known, values of X_{III} for the doped samples can alternatively be calculated with the equation given in Table I. Using $Z'=4$ and taking $S_A=0$, the X_{III} values thus calculated are found to be in the range of several times 10^{-3}, which are consistent with those listed in Table III, with the exception of that for the $\perp$-Y sample.

The stage-III conductivity of the $\perp$-Y sample seems anomalous at first glance. Its H_{III} value is almost twice that of the other doped crystals, while its X_{III} value is close to unity. One possible interpretation of these results is that the steep curve of the $\perp$-Y^{3+} sample is the only true stage III, while the more gentle low-temperature curves for the other doped samples are actually stage II. This interpretation, however, faces three difficulties: (a) it leaves no possible explanation for the decrease in slope above 150 °C observed in all doped samples except the $\perp$-Y one, (b) the values of the effective concentration X of these samples listed in Table III are inconsistent with those expected of stage-II values (viz., of the same order of magnitude as the dopant concentrations, or 10^{-4}), and (c) the effective concentration of the $\perp$-Y sample, $X=0.87$, is not consistent with that expected for stage-III behavior. Therefore we conclude that the curves with activation energy of 0.64–0.65 eV of the $\|$-Er, $\perp$-Er, and the $\|$-Y samples indeed represent stage III.

The anomalous steep slope for the $\perp$-Y sample can be explained, however, if one assumes the presence of a small amount of oxygen contaminant in this sample. The dopant in the sample would then be compensated not only by F_i, but also by substitutional oxygen, O_F. The charge-neutrality condition, Eq. (13), then has to be

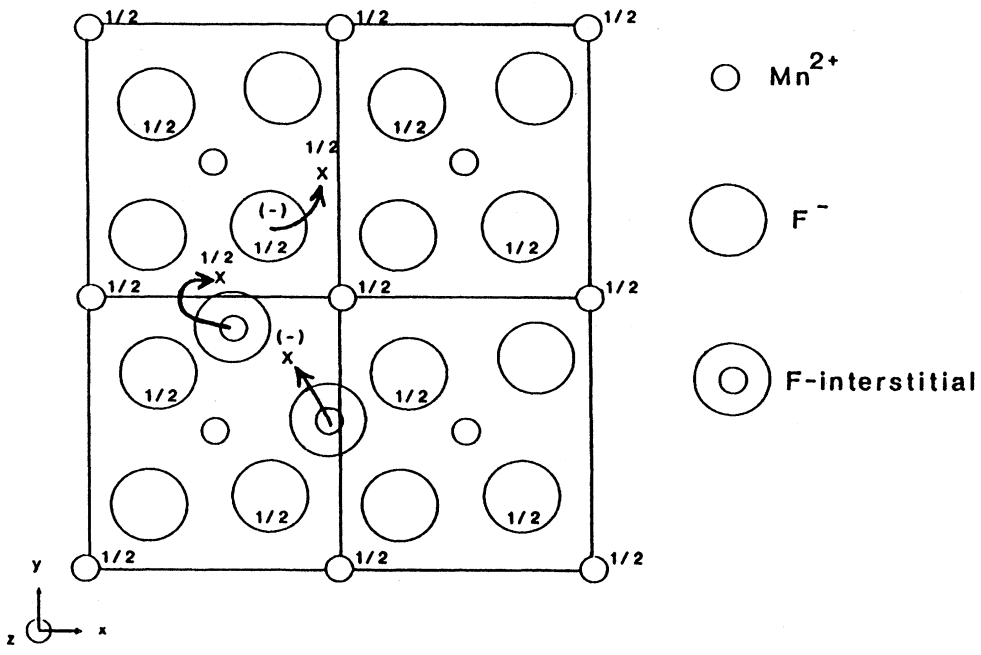

FIG. 11. The fluorine split-interstitial configuration of an isolated F_i in MnF_2 crystal. The arrows indicate the migration paths of the fluorine ions via the interstitialcy mechanism. The locations of the center of mass (i.e., center of charge) of the F_i pairs are indicated by the minus signs. The ions and the final positions that are located at one-half the c-lattice spacing above the basal plane are labeled $\frac{1}{2}$.

rewritten:

$$[D]=[F_i]+C_O \ , \tag{15}$$

where C_O is the mole fraction of the oxygen contaminant. In stage III almost all of the F_i are combined with D, so that $C_O \gg [F_i]$, i.e., the concentration of free fluorine interstitial. When Eq. (15) is then combined with Eq. (12), the modified stage-III activation enthalpy and effective concentration are found to be

$$H_{III}=H_A+H_m \ , \tag{16}$$

$$X_{III}=(Z')^{-1}[(C_D-C_O)/C_O]\exp(S_A/2k_B) \ . \tag{17}$$

In Eq. (16), H_{III} differs from that appearing in Table I in that H_A now appears without a factor of $\frac{1}{2}$. This difference can then explain the larger stage-III activation enthalpy observed for the $\perp$-Y sample. In addition, so long as C_O takes on values of a few ppm, both numerator and denominator of the second term of Eq. (17) have values in the ppm range. The result is that X_{III} has the order of magnitude of unity, again consistent with the observation made on the $\perp$-Y sample. Note that for this argument to be valid we require that C_O be large only compared to $[F_i]$, and not to C_D. In other words, only a very small amount of oxygen presence is needed for this anomalous behavior to occur. These results then imply that for the Y-doped samples only the $\perp$ sample, and not the $\parallel$ one, was contaminated with oxygen. Since the two samples were cut from different parts of the same mother crystal, this results could come about if there were an inhomogeneous oxygen distribution in this crystal. Unfortunately, we did not have another Y-doped MnF_2 crystal that would have permitted us to verify this hypothesis. Nevertheless, since this hypothesis provides the only reasonable interpretation of all the data, we shall assume that it is correct.

It is interesting to note the oxygen contaminant is expected to enter the solid solution by subsitituting for fluorine ion, i.e., in the form of O_F. Its compensating defect, irrespective of whether the intrinsic disorder is of the anion Frenkel or Schottky type, would then be the fluorine vacancy, V_F. This is precisely the defect required to produce oxygen diffusion via the vacancy-migration mechanism. The trivalent cation dopant D carries an effective charge of $1+$. It is of the same sign as that of V_F, so that the presence of the cation dopant suppresses the V_F concentration and, in turn, hinders oxygen from diffusing into the crystal. This may explain why irreversible increases in conductivity are found in the pure samples but not in the doped samples. The fact that the $\perp$-pure sample did not show as much conductivity increase as the $\parallel$-pure one (see Fig. 9) also indicates the oxygen has a lower diffusivity in the $\perp$ than in the $\parallel$ direction. This observation is very similar to that found in the MgF_2 system.[9]

The fact that the values of H_{III} are similar in the $\parallel$ and $\perp$ Er-doped samples means that the H_m values of the fluorine interstitial in the two orientations are very close to each other. This observation can be accounted for by either one of the following two different models on F_i migration. In the first model a single F_i jump contributes to conductivities in both orientations, so that the corresponding H_m values are identical. In the second model the F_i migrates with two different jumps in $\parallel$ and $\perp$ orientations, respectively, but by coincidence, these jumps have very similar activation enthalpies. Computer-simulation calculations[18] suggested that both models are possible. The calculations carried out on an isolated F_i showed that there are three interstitial configurations (viz., tetrahedral, octahedral, and split interstitial) that are stable and have similar energies with the split interstitial marginally favored over the others. The implication of this finding is that the F_i may go from one of these configurations into another very easily. This suggests an interstitialcy mechanism as shown in Fig. 11, which has as its transition state the F_i sitting either at the tetrahedral or octahedral site. This migration mode has both $\parallel$ and $\perp$ components and fits the description of the first model. Since this jump involves the combined motion of three F_i's, an estimate of the upper bound of its activation energy can be obtained from the largest activation energy of the individual F_i jumps. According to the calculations, this value is given by the 0.19 eV for the F_i movement in the $\parallel$ direction, and agrees well with the experimental value of 0.10 eV which will be shown to be the case in the later part of this paper. For the second mode, the same calculations resulted in migration energies of 0.12 and 0.19 eV for F_i migrations along the c axis and in the basal plane, respectively, with a difference of only 0.7 eV between them. In order to decide between these two models, we have calculated from them their respective conductivity anisotropy ratios and compared them with the experimental value. The expression for this ratio is obtained by applying Eqs. (8) and (9) to both orientations and is found to be

$$\sigma_\parallel/\sigma_\perp=2(d_\parallel^2/d_\perp^2) \ , \tag{18}$$

where the subscripts indicate the orientations of the corresponding quantities, and the factor 2 comes from the geometric factor β. For the first mode, using $d_\parallel=1.65$ Å and $d_\perp=3.52$ Å, this ratio is calculated to be 0.44. These d values are that of the components of the jump distance, along and perpendicular to the c axis, respectively, between the two negative charge centers shown in Fig. 11. For the second model, on the other hand, the d values used are obtained from the F_i migration paths considered in the calculation. These are $d_\parallel=3.31$ Å (which is the lattice constant c), and $d_\perp=3.52$ Å. The corresponding conductivity anisotropy ratio is then found to be 1.76 for the second model. Clearly, only the ratio obtained from the first model agrees reasonably well with the experimental value of approximately 0.30 (measured at $10^3/T=3.2\ K^{-1}$ in Fig. 8 for the Er-doped samples). Thus it is concluded that the F_i migrates with an interstitialcy mechanism.

The expression for H_{III} given in Table I yields, when inserting the experimental value for the Er-doped samples in either the $\parallel$ or $\perp$ orientations,

$$0.64 \text{ eV}=H_A(\text{Er})/2+H_m \ , \tag{19}$$

TABLE IV. Summary of the various enthalpy values obtained.

Enthalpy	Defect and/or defect complex	Value (eV)
Association enthalpy H_A	ErF_i	1.08
	YF_i	1.10
Migration enthalpy H_m	F_i	0.10
Formation enthalpy H_f	V_F+F_i	3.56±0.02

where H_A(Er) is the association enthalpy of the defect pair involving the Er dopant. For the Y-doped samples, the following equations are obtained for the two differently oriented samples [utilizing Eq. (16) for the ⊥ case]:

$$0.65 \text{ eV}=H_A(\text{Y})/2+H_m \ , \tag{20}$$

$$1.20 \text{ eV}=H_A(\text{Y})+H_m \ . \tag{21}$$

Note that the same H_m is used in all three equations, since, in all cases, it is the migration enthalpy of F_i via the interstitialcy mechanism. Solving these equations, one obtains the numerical values for H_A and H_m listed in Table IV.

These values seem reasonable when compared to those obtained from computer-simulation calculations,[18] which yield 0.97 and 0.77 eV for H_A(Er) and H_A(Y), respectively, and 0.1–0.7 eV for activation energy of the F_i migration. The good agreement of these numbers also provides further support for our earlier assumption that the ⊥-Y sample is influenced by oxygen contamination.

The conductivity curves of both the ∥ and ⊥-pure samples came together at high temperature (see Fig. 8). This give rise to the possibility that the high-temperature stages of these samples are truly the stage-I region. To check this possibility, the value of the formation entropy factor is calculated from the effective concentrations listed in Table III, X_I with the equation in Table I. It is further noticed that the ⊥ sample shows a much longer straight-line region at high temperature, and thus provides the more accurate value of X_I. The formation entropy thus obtained from the preexponential of the ⊥ sample is $S_f/k_B=5.4$, which is quite reasonable for such a Frenkel defect.[31] Thus it is concluded that the high-temperature stage in the pure sample is consistent with a stage-I interpretation.

The value of H_I listed in Table III falls in the range of 1.87±0.02 eV. Assuming F_i to be the dominant defect charge carrier in stage I, the expression for H_I is given in Table I. Since H_m was determined earlier to be 0.10 eV, the formation enthalpy of the anion Frenkel pair is then found to be $H_f=3.56\pm0.02$ eV. We compare this with the calculated anion Frenkel formation energy of 2.92 eV obtained from computer simulation[18] and find the agreement quite acceptable considering the uncertainties in the calculation.

VI. CONCLUSIONS

It is noteworthy that in the present work, by studying the anisotropic properties of MnF_2 crystals, we are able to obtain important information leading to a defect model, as well as to some explicit quantitative results. The defect model is a self-consistent one in that it explains our various experimental observations on the doped as well as the pure MnF_2 crystals in both the ∥ and ⊥ orientations. The more important findings of this work are summarized below.

(i) The intrinsic defect of crystalline MnF_2 is the anion Frenkel defect.

(ii) The trivalent cation dopants in MnF_2 are compensated by the fluorine interstitial F_i. At moderate temperatures they combine to form neutral defect pairs in which the F_i is in a low-symmetry split-interstitial configuration. This configuration gives rise to the dielectric-loss peaks observed at cryogenic temperatures.

(iii) The predominant charge carrier that contributes to the conductivity is the F_i, which has a split configuration and migrates by the interstitialcy mechanism.

(iv) The various enthalpy values obtained are listed in Table IV.

ACKNOWLEDGMENTS

This work was supported by the U.S. Department of Energy under Grants No. DE-FG02-85ER34187 and No. DE-FG02-88ER45341. The authors are also grateful to Professor A. N. Cormack and Professor C. R. A. Catlow for helpful discussions.

*Present address: Corporate Research Science Laboratories, Exxon Research and Engineering Company, Clinton Township, Route 22 East, Annandale, NJ 08801.

[1]A. B. Lidiard, in *Handbuch der Physik* (Springer-Verlag, Berlin, 1957), Vol. 20, p. 246.

[2]R. G. Fuller, in *Point Defects in Solids,* edited by J. H. Crawford, and L. M. Slifkin (Plenum, New York, 1972), Vol. 1, Chap. 2.

[3]R. J. Friauf, in *Physics of Electrolytes,* edited by J. Hladik, (Academic, London, 1972), Vol. 1, Chap. 2.

[4]F. Béniére in Ref. 3, Vol. 1, Chap. 6.

[5]A. B. Lidiard, in *Crystals with the Fluorite Structure,* edited by W. Hayes (Clarendon, Oxford, 1974), p. 101.

[6]W. J. Fredericks, in *Diffusion in Solids,* edited by A. S. Nowick, and J. J. Burton (Academic, New York, 1975), Chap. 8.

[7]A. V. Chadwick, Radiat. Effects **74**, 17 (1983).
[8]J. F. Nye, *Physical Properties of Crystals* (Oxford University Press, London, 1957).
[9]D. S. Park and A. S. Nowick, J. Phys. Chem. Solids **37**, 607 (1976).
[10]J. Toulouse and A. S. Nowick, J. Phys. (Paris) Colloq. **41**, C6-243 (1980).
[11]J. Toulouse and A. S. Nowick, Radiat. Effects **75**, 41 (1983).
[12]K. K. Kim and A. S. Nowick, J. Phys. C **10**, 509 (1977).
[13]K. K. Kim, J. Toulouse, and A. S. Nowick, Phys. Status Solidi B **93**, K1 (1979).
[14]T. A. Roth, J. Appl. Phys. **42**, 246 (1971); **44**, 1056 (1973).
[15]A. S. Nowick, J. Appl. Phys. **44**, 5169 (1973).
[16]J. Toulouse, A. S. Nowick, and L. E. Halliburton, Phys. Rev. B **26**, 2926 (1982).
[17]C. R. A. Catlow, R. James, and M. J. Norgett, J. Phys. (Paris) Colloq. **37**, C7-443 (1976).
[18]A. N. Cormack, C. R. A. Catlow, and S. Ling, this issue, the following paper, Phys. Rev. B **40**, 3278 (1989).
[19]A. S. Nowick and W. R. Heller, Adv. Phys. **14**, 101 (1965).
[20]A. S. Nowick, in Ref. 2, Chap. 3.
[21]E. Weinberg and N. K. Srinivasan, J. Cryst. Growth, **26**, 210 (1974).
(1974).
[22]J. R. Macdonald, *Impedance Spectroscopy* (Wiley, New York, 1987).
[23]E. J. L. Schouler, in *Solid State Protonic Conductors III for Fuel Cells and Sensors: Proceedings of European Workshop,* edited by J. B. Goodenough, J. Jensen, and A. Potier (Odense University Press, Odense, Denmark, 1985).
[24]J. M. Hodge, M. D. Ingram, and A. R. West, J. Electroanal. Chem. **74**, 125 (1976).
[25]J. R. Macdonald, in *Electrode Processes in Solid State Ionics,* edited by M. Kleitz and J. Dupuy (Reidel, Dordrecht, 1976), p. 149.
[26]F. Bridges, CRC Crit. Rev. Solid-State Sci. **5**, 1 (1975).
[27]J. Toulouse, S. Ling, and A. S. Nowick, Phys. Rev. B **37**, 7070 (1988).
[28]J. R. Neighbours and R. W. Moss, Phys. Rev. **173**, 542 (1968).
[29]A. S. Nowick and B. S. Berry, *Anelastic Relaxation in Crystalline Solids* (Academic, New York, 1980), p. 216.
[30]C. R. A. Catlow, M. Dixon, and W. C. Mackrodt, in *Computer Simulation of Solids,* edited by C. R. A. Catlow and W. C. Mackrodt (Springer-Verlag, Berlin, 1982), Chap. 10.
[31]A. D. Franklin, in Ref. 2, Chap. 1.